Water-Accelerated Transport: Vapor-Phase Nerve Agent Simulant Delivery within a Catalytic Zirconium Metal−Organic Framework as a Function of Relative Humidity

Rui Wang,[‖] Kaihang Shi,[‖] Jian Liu, Randall Q. Snurr,* and Joseph T. Hupp*

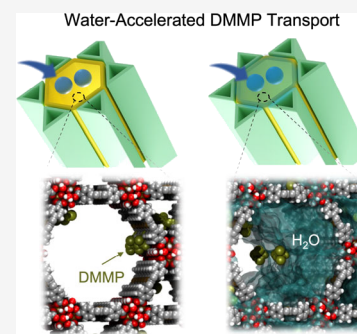ACCESS | 📊 Metrics & More | 📖 Article Recommendations | 🆂🅸 Supporting Information

ABSTRACT: Zirconium-based metal−organic frameworks (MOFs) are candidate materials for effective nerve agent detoxification due to their thermo- and water stability as well as high density of catalytic Zr sites. However, as high-porosity materials, most of the active sites of Zr-MOFs can only be accessed by diffusion into the crystal interior. Therefore, the transport of nerve agents in nanopores is an important factor in the catalytic performance of Zr-MOFs. Here, we investigated the transport process and mechanism of a vapor-phase nerve agent simulant, dimethyl methyl phosphonate (DMMP), through a representative Zr-MOF, NU-1008, under practical conditions of varying humidity. Confocal Raman microscopy was used to monitor the transport of DMMP vapor through individual NU-1008 crystallites, where the relative humidity (RH) of the environment was tuned to understand the impact of water. Counterintuitively, water in the MOF channels, instead of blocking DMMP transport, assists DMMP diffusion; indeed, the transport diffusivity (D_t) of DMMP in NU-1008 is one order of magnitude higher at 70% than 0% RH. To understand the mechanism, magic angle spinning NMR and molecular dynamics simulations were performed and suggested that high water content in the channels prevents DMMP from hydrogen-bonding with the nodes, allowing for faster diffusion of DMMP in the channels. The simulated self-diffusivity (D_s) of DMMP is observed to be concentration-dependent. At low loading of DMMP, D_s is higher at 70% RH than 0% RH, while at high loadings the trend reverses due to the DMMP aggregation in water and the reduction of free volume in channels.

Water-Accelerated DMMP Transport

INTRODUCTION

Metal−organic frameworks (MOFs), which are assembled by linking metal nodes and organic linkers, typically feature high porosity, along with crystallinity and extensive structural tunability.[1,2] These characteristics have rendered MOFs attractive candidates for catalysis applications, such as conversion of small hydrocarbons (natural gas) into feedstocks for chemical manufacturing[3] or detoxification of chemical weapons.[4,5] The high porosity of many MOFs implies that the majority of the active sites are housed in the interiors of particles/crystallites.[6] The ability to access active sites located within pores can partially or fully determine the extent of utilization, and the overall performance, of MOF-based catalysts.[7−10] Therefore, the transport of guest molecules into and through MOFs should be investigated to fully understand the catalytic processes and to guide the development of transport-efficient new MOFs for chemical catalysis.[11] For MOF-enabled catalytic reactions occurring on and within crystallites enshrouded by ambient air of finite humidity, a commonly overlooked consideration is the recruitment of atmospheric water by MOFs.[12,13] Indeed, numerous MOFs have been found capable of capturing water from air and, depending on relative humidity, concentrating it to liquid-like levels.[14−17] At these concentrations, sorbed water might well

diminish or block the transport of reactants and products, thereby impacting catalytic efficacy.

Zr-MOFs, featuring high water and thermal stability, have shown promise for adsorption and detoxification of nerve agents such as sarin and soman.[18] The catalytic activity originates from the Lewis-acidic Zr(IV) nodes, which are excellent in activating the organophosphates by binding to the P=O group, with detoxification ultimately occurring by the hydrolysis of P−F bonds (or for simulants, P−O bonds).[19] For example, Mondloch *et al.*[18] have reported that NU-1000, which can present up to four such sites per Zr node, can rapidly degrade nerve agent simulants in aqueous buffer solution, *e.g.*, initial half-lives for hydrolytic detoxification as brief as 1.5 min. The fast catalytic kinetics make Zr-MOFs promising candidates to be integrated into respirators and clothing for human protection.[20−22] While free water molecules are not required for stoichiometric capture and degradation of simulants[23,24] or agents by a Zr-MOF, catalytic degradation
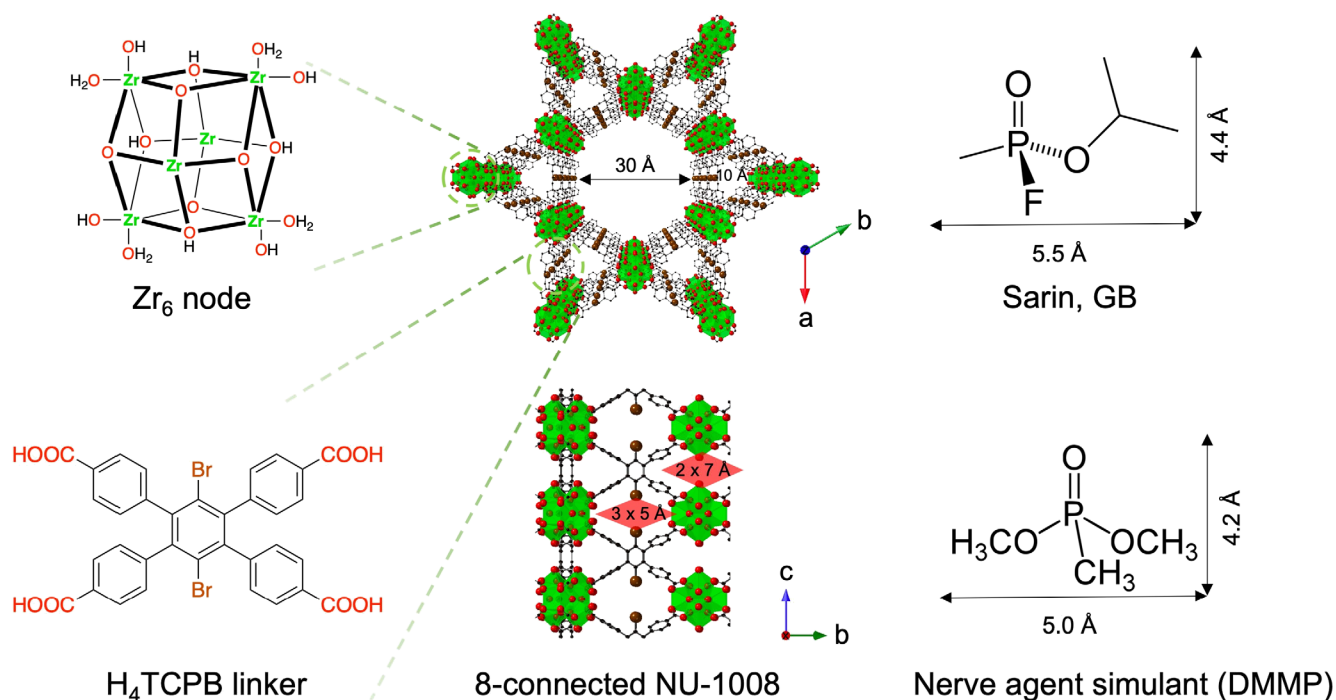
Figure 1. Composition and structure of Zr-MOF NU-1008 (a, b, and c represent the crystallographic axes). Structures and dimensions of a nerve agent (sarin) and its simulant (DMMP).
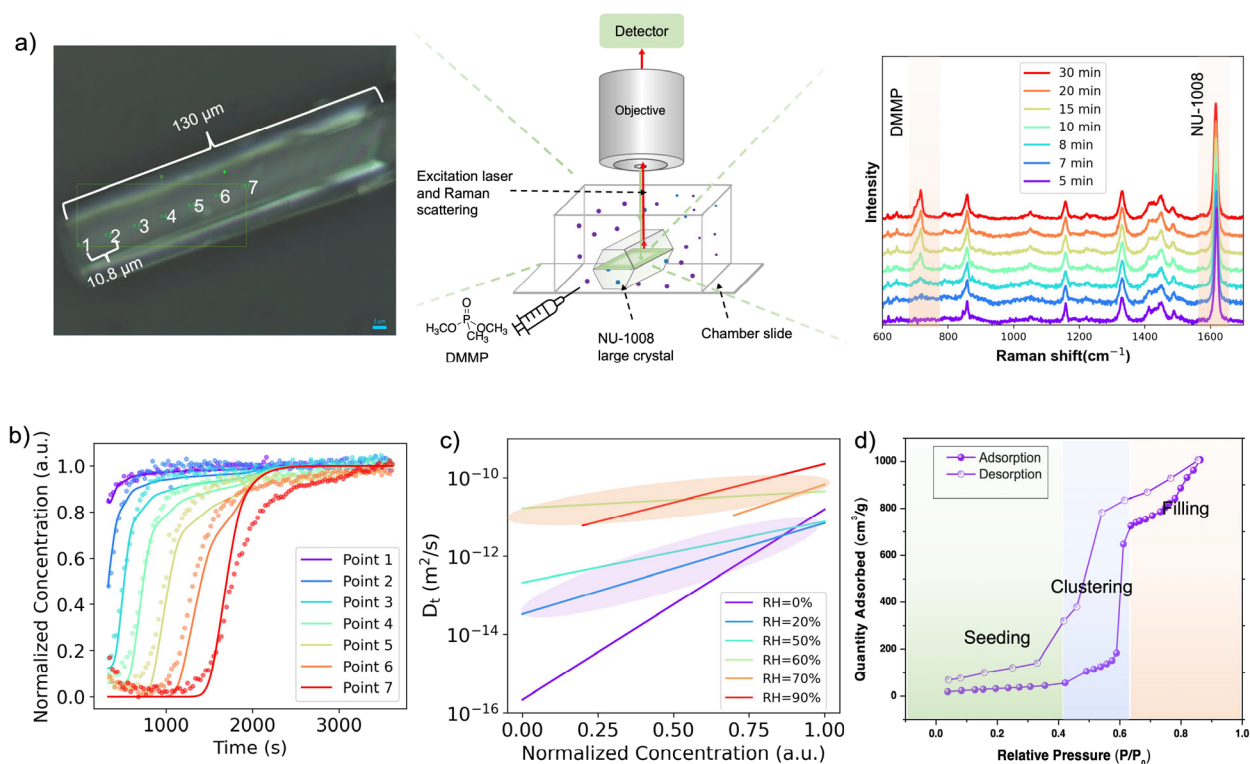

Figure 2. Non-equilibrium transport of DMMP in NU-1008. (a) Schematic representation of the confocal Raman microscopy (CRM) setup for monitoring vapor-phase DMMP transport through NU-1008 large crystals. The optical image shows NU-1008 crystal morphology and the locations where DMMP concentrations were monitored. The Raman signals from both DMMP and NU-1008 at the crystal center are shown as a function of time. (b) Spatially resolved concentration evolution of DMMP in NU-1008 as a function of time at 0% RH. Points are experimental data, and curves are Fickian fittings. Equivalent transient concentration profiles plotted versus position at different times are shown in Figure S6. Fittings at other RHs are available in Figure S8. (c) Transport diffusivity D_t of DMMP in NU-1008 under different relative humidities. The distribution of D_t is shaded in purple and orange for low RH and high RH, respectively. (d) Water sorption isotherm of NU-1008 at 25 °C. Background sections shaded in green, blue, and orange represent seeding, clustering, and filling stages, respectively.

requires an accessible reservoir of water molecules. Water sorption within MOF pores constitutes a reservoir. However, Wang et al.[25] reported that the detoxification of simulants and real agents deposited directly (as neat liquids) on Zr-MOFs positioned in a lab atmosphere is less efficient than detoxification accomplished by Zr-MOFs immersed in a solution containing a dissolved simulant or agent. They additionally reported that the extent of water loading in the *ex situ* MOF can affect the reaction rate.[13] One plausible interpretation is that co-adsorption of water favorably alters the mechanism of simulant or agent transport, thereby enhancing overall rates for hydrolytic degradation.[26,27] There are, however, very few quantitative, experimental, mechanistic reports on nerve agent (or simulant) transport in MOFs, especially in the presence of water.[28]

Hence, we investigated the transport process and mechanism of a vapor-phase nerve agent simulant, dimethyl methyl phosphonate (DMMP), through a representative Zr-MOF NU-1008 (Figure 1). Confocal Raman microscopy was used to monitor DMMP transport spatially and temporally under non-equilibrium conditions, where the relative humidity was varied from 0 to 90% to study the impact of water. Counterintuitively, more water in the MOF channels facilitates DMMP transport, and the transport diffusivity of DMMP in water-filled NU-1008 is one order of magnitude higher than that in empty pores. To further understand the transport mechanism, magic angle spinning (MAS) NMR and molecular dynamics (MD) simulations were performed, where, at low relative humidity (RH ≤ 50%), the P=O group of DMMP was observed to preferentially bind with Zr nodes via hydrogen bonding, while in water-filled channels where water molecules surround the node, the hydrogen bonding between DMMP and the node is interrupted, which increases the mobility of DMMP.

METHODS

Material Synthesis and Characterization. NU-1008 rod-shaped crystals were solvothermally synthesized with $ZrCl_4$ and 1,2,4,5-tetrakis(4-carboxyphenyl)-3,6-dibromo-benzene (H_4TCPB) linker using a previously reported method.[27] Both large crystals (300 μm in length) and powder crystals (3 μm in length) were made by tuning the formic acid and solvents (see the Supporting Information for details). The as-synthesized samples were activated by supercritical CO_2 to remove the residual solvents in the pores before further characterization and measurements (see the Supporting Information for details). Powder X-ray diffraction (PXRD) patterns were collected for both large and small NU-1008 crystals to confirm the crystallinity and phase purity. A N_2 isotherm was measured to obtain the surface area and pore size distribution of NU-1008. A H_2O isotherm was also collected to assist in understanding the water filling process in the NU-1008 pores. The Zr_6-node structure of NU-1008 was characterized by collecting the diffuse reflectance infrared Fourier transform spectroscopy (DRIFTS) spectra.

DMMP Transport Monitored by Confocal Raman Microscopy. To understand the transport process of DMMP through Zr-MOF NU-1008, a confocal Raman microscope[29−31] (see the Supporting Information Section S3 for details) was used to monitor DMMP vapor transport through individual NU-1008 crystals as a function of time and location (Figure 2a). NU-1008 rod-shaped crystals (150−300 μm in length), which were pre-equilibrated in a mini-glovebox under different relative humidities (RH = 0, 20, 50, 60, 70, and 90%), were sealed in chamber slides, which would be mounted on the confocal Raman microscope for transport monitoring (Figure 2a). DMMP liquid was then injected into the chamber slide (volume, ~125 μL), which allowed for a stable DMMP vapor pressure surrounding the NU-1008 crystals. After injection, a NU-1008 crystal central layer was immediately focused by translating the microscope

stage in the x,y-direction and the objective in the z-direction. Seven different locations on the crystals covering half of the crystal length were selected through a 50× microscope for mapping. Laser light (532 nm) was used to excite the samples. The Raman spectra (Raman shift, 600−1700 cm⁻¹) at each location were collected at 30 s intervals to follow DMMP accumulation and distribution in the NU-1008 crystals (see the Supporting Information for details).

Molecular Mobility Investigated by Magic Angle Spinning NMR. To understand the structure of water and DMMP molecules adsorbed in MOF, ¹H NMR and ³¹P MAS NMR were performed on a Bruker 400 MHz instrument with a 4 mm HX probe. Before measurements, NU-1008 powder was equilibrated in the mini-glovebox under representative relative humidities (RH = 0, 20, 60, and 70%), and then half of the samples were exposed to saturated DMMP vapor for 24 h for adsorption. The water-only MOF samples and DMMP-adsorbed MOF samples were then loaded and sealed in a 4 mm zirconia rotor to perform the ¹H and ³¹P MAS-NMR measurements.[32,33] For ¹H MAS NMR, a total of 16 scans were recorded at a spin rate of 14 kHz at the magic angle to distinguish individual peaks of protons. For the ³¹P MAS-NMR spectra, a total of 64 scans were performed at a spin rate of 14 kHz at the magic angle to achieve high-quality spectra. The transverse relaxation time (T_2) of ³¹P was measured by the Carr-Purcell-Meiboom-Gill (CPMG) pulse sequence.[34] A spin rate of 14 kHz and 128 scans were applied for measurements.

Fickian Analysis for Transport Diffusivity and Surface Permeability. Spectroscopic band analysis was performed on the Raman spectra to quantify the concentration of DMMP in NU-1008 at different locations as a function of time. First, baseline corrections were applied to regions of the spectra containing the Raman bands of interest (600−1700 cm⁻¹). Then, the Raman bands used for quantification were fitted to Gaussian functions using the highest signal-to-noise spectrum acquired for each kinetic series. These functions were amplitude-scaled to fit all other spectra in the series and integrated to determine peak areas for quantification (peak area of ν_{p-c} (A_{DMMP}) and ν_{coo^-} ($A_{NU-1008}$)). DMMP intensity (I) was calculated by $A_{DMMP}/A_{NU-1008}$. The intensity data were normalized to a concentration c by $c = (I - I_{min})/(I_{max} - I_{min})$, where I_{min} and I_{max} are the minimum and equilibrium intensities, respectively.

Assuming that the diffusion of DMMP into the NU-1008 crystal follows one-dimensional (1D) diffusion behavior along the axial z-direction of the channel (*i.e.*, crystallographic c-axis in Figure 1), the transport diffusivity D_t and surface permeability α of the system can be obtained by fitting the experimental diffusion data to Fick's second law:[35]

$$\frac{\partial c}{\partial t} = \frac{\partial}{\partial z}\left(D_t \frac{\partial c}{\partial z}\right) \tag{1}$$

where normalized concentration $c(z, t)$ is a function of the axial position z along the 1D crystal channel and time t. The solution of eq 1 is subject to two boundary conditions:

$$D_t \frac{\partial c}{\partial z} = 0 \text{ at } z = 0 \text{ (center of the crystal)} \tag{2}$$

$$D_t \frac{\partial c}{\partial z} = \alpha(c_{eq} - c_s) \text{ at } z = l \text{ (crystal edge)} \tag{3}$$

Equation 2 indicates that there is no net flux at the center of the crystal due to the symmetry of the channel, which ranges from [− l, l]. Equation 3 describes the effect of transport resistance on the crystal external surface, where c_{eq} is the adsorbed phase concentration at equilibrium with the surrounding phase, $c_s = c (z = l, t)$ is the actual adsorbed phase concentration just inside the crystal, and l is the half length of the crystal. Here, we hypothesized that both the transport diffusivity $D_t(c)$ and surface permeability $\alpha(c_s)$ are concentration-dependent. In this case, no analytical solution to eq 1 is possible. Instead, we can write a finite difference solution to Fick's second law.[36,37] The surface permeability $\alpha(c_s)$ was first numerically evaluated using Fick's 1st law and the boundary condition in eq 3.[37] With $\alpha(c_s)$, the transport diffusivity $D_t(c)$, which is assumed to be an exponential
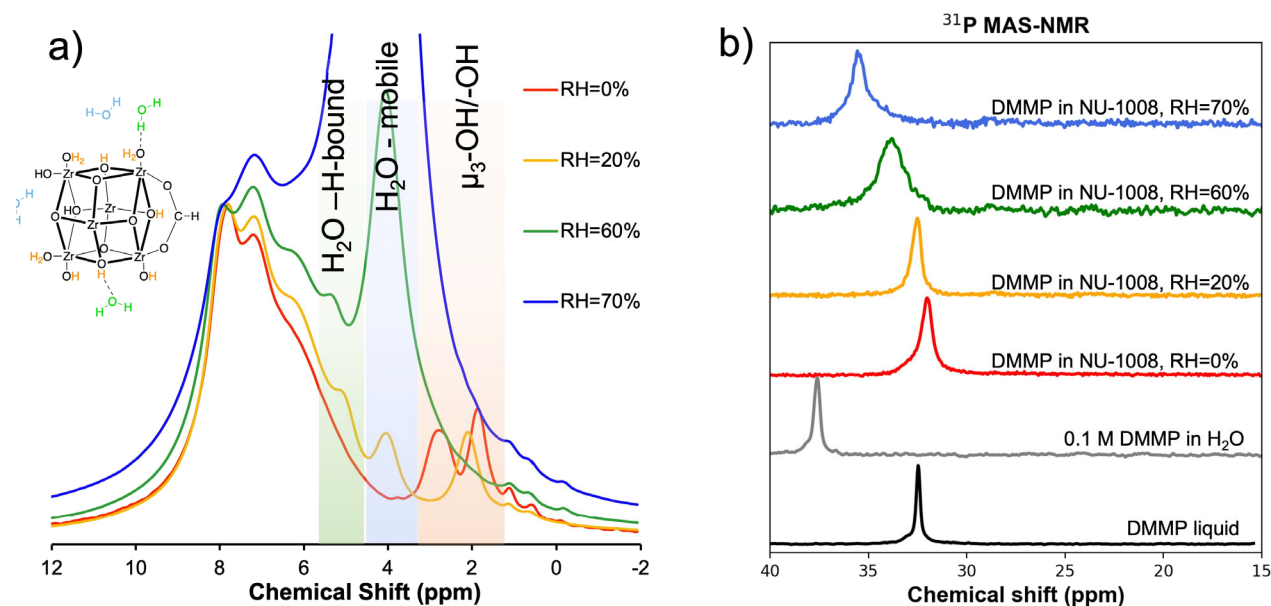
Figure 3. (a) Evolution of water structures in NU-1008 identified by ss-NMR. (b) ^{31}P MAS NMR of DMMP adsorbed in NU-1008 samples that were pre-equilibrated under different RH values.

function of the concentration, was fitted by minimizing the root mean square error between the experimental data and the predictions using the Fickian finite difference equations. Further details on the Fickian diffusion analysis are available in Section S4.1. Python Jupyter notebooks for performing this Fickian fitting under different RH conditions are provided in the Supporting Information.

Equilibrium Molecular Dynamics Simulations. Canonical (NVT) molecular dynamics (MD) simulations were performed using LAMMPS software (version 3 Mar 2020).[38] We investigated DMMP diffusion in NU-1008 under representative RH conditions (RH = 0, 20, and 70%) and DMMP loadings at 298 K.[39] The DMMP molecule was modeled using the united-atom TraPPE force field.[40,41] The water molecule was simulated using the rigid TIP4P/2005 force field.[42] During the simulations, the framework structure was assumed to be rigid. Nonbonded interaction parameters for framework atoms were taken from a mixed set of force fields, DREIDING,[43] UFF,[44] TraPPE,[45] and TIP4P/2005,[42] following the suggestions of Wardzala et al.[46] Partial charges of framework atoms were assigned by the PACMOF tool.[47] For each RH condition, the number of water molecules in the simulation was fixed at the value from the experimental water adsorption isotherm (Figure 2d). All nonbonded interactions were spherically truncated at 14 Å with no tail corrections. The long-range Coulombic interactions were handled using the particle-particle particle-mesh (PPPM) method with a computation accuracy of 1×10^{-6}.[48,49] Lorentz-Berthelot (arithmetic) combining rules were applied to estimate the cross-interaction parameters for unlike pairs.

The starting configuration for the MD simulation was generated using RASPA2 software,[50] where an initially random water/DMMP configuration in a $(1 \times 1 \times 3)$ NU-1008 supercell was quickly thermalized by a NVT Monte Carlo(MC) simulation. Periodic boundary conditions were applied in all directions. The number of degrees of freedom for the simulation was set to $3N$, treating the rigid framework as an external field.[51] The system was integrated using the velocity Verlet algorithm with a timestep of 1 fs. All MD simulations were first equilibrated for 2 ns, and statistics were collected in the following 100 ns. The self-diffusivity of DMMP, D_s, was calculated from the mean square displacement (MSD) of the phosphorus atom using the Einstein relation. We used a robust and automated workflow to fit the MSD and to determine D_s in the long-time limit (the diffusive regime).[52] For each reported D_s, we took an average from three independent MD simulations with different initial velocity distributions. Further simulation details can be found in Section S6.

Example simulation files and Python scripts for the D_s calculations are available in the Supporting Information.

RESULTS AND DISCUSSION

Material Characterization. The PXRD patterns of the NU-1008 powder and large crystals match with the patterns from single-crystal analysis (Figure S1a), confirming the structure and phase purity of both samples. The N_2 isotherm of NU-1008 powder measured at 77 K shows a type IV isotherm (although there is no hysteresis), consistent with the existence of both mesopores and micropores (Figure S1b).[53] The BET area is calculated to be 1365 m^2/g. A DFT pore size distribution calculation reveals that the mesopore diameter is 30 Å and the micropore diameter is 11 Å (Figure S1c), which are both wide enough for DMMP transport along the c-direction of the crystal (Figure 1). The windows interconnecting the different channels are small as shown in Figure 1, which likely limits the path of DMMP and leads to primarily 1-D transport. The DRIFTS and ^{1}H NMR spectra were used to characterize the node structure of NU-1008.[54] The peak at 3672 cm^{-1} is assigned to O−H stretching from terminal aqua or hydroxyl ligands ($-H_2O/-OH$) located on the Lewis acidic Zr site, which are potential binding sites for the P═O group in DMMP. Note that the peak at 2745 cm^{-1} is attributed to C−H vibration from node-ligated formate (Figure S2).[55] Adventitious formate originated from aq. HCl-facilitated thermal degradation of DMF during the modulator-removal step of the solvothermal synthesis.[56] ^{1}H NMR of the dissolved MOF confirmed the presence of formate, with a loading of ~3/node (Figure S4), implying the initial presence of one terminal-OH/ H_2O pair per node. Presumably, formate dissolves in water when water appears in pores. Curiously, water introduction at 60 or 70% RH is accompanied by the disappearance of μ_3-OH protons at 2.8 ppm in the ^{1}H MAS NMR spectra of NU-1008 (Figure 3a). Spontaneous deprotonation of bridging-hydroxo ligands above a threshold level of water infiltration is not unexpected in view of the acidity of these ligands (pK_a = ~3.3).[57]
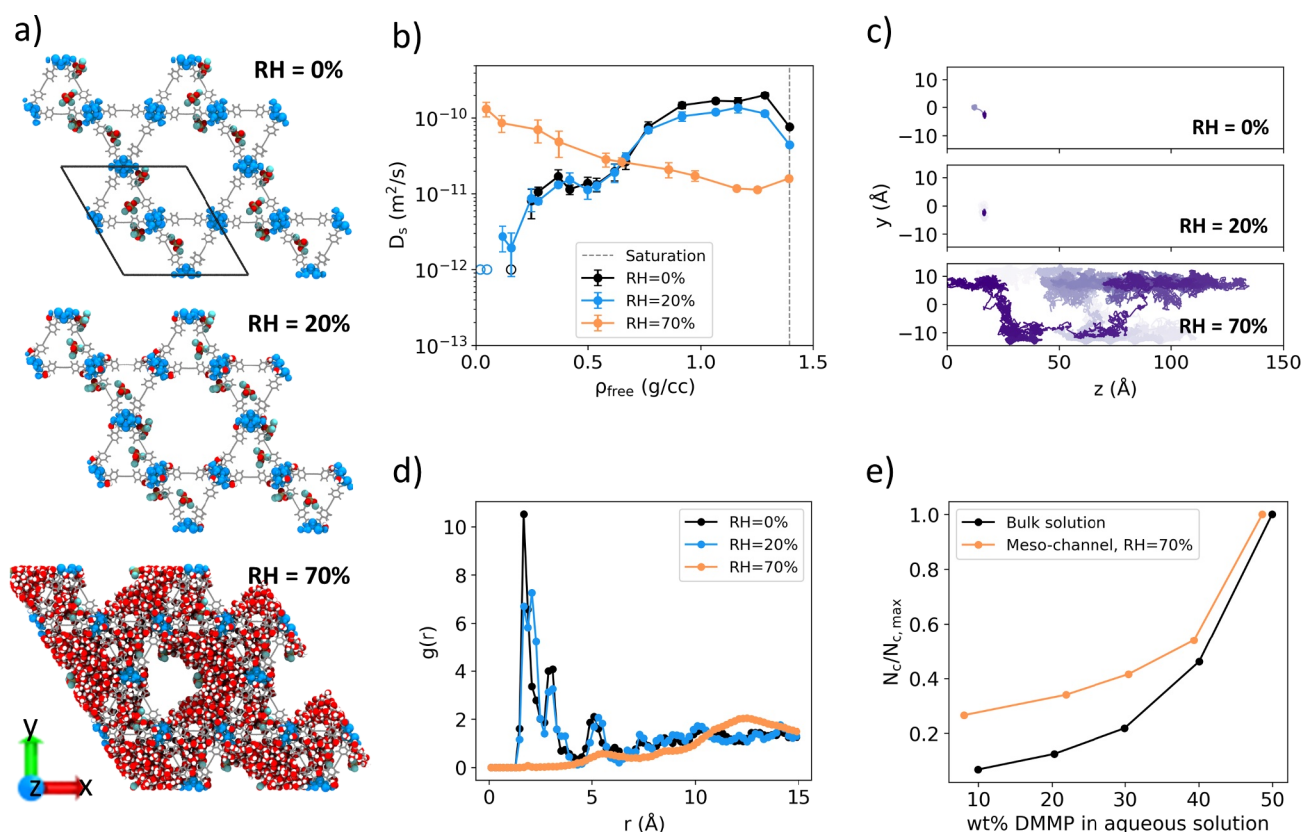
Figure 4. MD simulation results for DMMP diffusion in NU-1008 under three representative RH conditions. (a) Representative simulation snapshots at low loading of DMMP ($\sim$1 DMMP per unit cell). The black box indicates the size of the unit cell. Gray: linkers of NU-1008; blue: node atoms; white: hydrogen; red: oxygen; cyan: methyl group; tan: phosphorus. (b) Self-diffusivity D_s of DMMP in the meso-channel versus free pore density in the meso-channel, ρ_{free}, which is defined as the mass of DMMP molecules per unit free volume in the meso-channel (see Section S6.7 for details). The estimated saturation density in the meso-channel (gray vertical dashed line) is $\rho_{free,\,sat} \approx 1.39$ g/cc, which was obtained from grand canonical Monte Carlo simulation (Figure S16). Open markers with a fixed value of 10^{-12} m^2/s correspond to D_s values that are smaller than 10^{-12} m^2/s and are thus inaccessible to the current MD timescale (100 ns). Error bars are the sample standard deviation. (c) Single-molecule trajectory of DMMP on the yz-plane in the meso-channel at low loading of DMMP ($\rho_{free} \approx 0.03$ g/cc or 0.67 DMMP in the meso-channel per unit cell); z-direction is parallel to the axial direction of the channel. The color map from light purple to dark purple denotes the simulation time from 0 to 100 ns. (d) Radial distribution function, $g(r)$, between hydrogen atoms of the node and oxygen atoms of DMMP at the same loading as panel (c). (e) Normalized average size of DMMP aggregates in bulk solution and in the meso-channels of NU-1008 at RH = 70%, where N_c is the average number of DMMP molecules in an aggregate and $N_{c,\,max}$ is the largest average number of DMMP in an aggregate. The values of $N_{c,\,max}$ are 22 for the bulk solution and 4 for the meso-channel (at saturation). We note that these absolute values depend on the system size, so the normalized amounts presented here can, to some extent, eliminate the effect of the system size.

DMMP Transport through NU-1008 under Non-equilibrium Conditions at Different Relative Humidities. Two characteristic peaks from NU-1008 and DMMP were identified for quantitative CRM analysis (Figure S5a).[58] The peak area of the P−C vibration mode of DMMP (712 cm^{-1}, A_{DMMP}) relative to that of the COO$^-$ group of NU-1008 (1612 cm^{-1}, $A_{NU-1008}$) increased as the DMMP vapor exposure time increased (Figure 2a), indicating DMMP accumulation inside the MOF. The DMMP normalized concentrations in NU-1008 obtained from the intensity $I = A_{DMMP}/A_{NU-1008}$ at different crystal locations (Figure 2b) provided two immediate insights into the transport process: (1) The DMMP concentration at the crystal edge (point 1) did not reach equilibrium at the beginning of the exposure to DMMP, indicating the existence of surface barriers at the channel termini. (2) The closer to the crystal center, the longer the induction period of DMMP accumulation, suggesting that intracrystalline diffusion resistance also played a critical role in the transport process. Note that no DMMP degradation was

observed during the transport process under these measurement conditions (Figure S5b).

To gain a quantitative understanding of the diffusion behavior of DMMP in NU-1008, a 1D Fickian diffusion model that incorporates a surface barrier at the crystal boundaries was implemented to extract the intracrystalline transport diffusivity $D_t(c)$ and the surface permeability $\alpha(c_s)$ from the experimental concentration profiles.[59] Figure 2b shows spatially resolved concentration profiles of DMMP at distinct locations under 0% RH. The good agreement between the Fickian fittings (curves) and the experimental data (points) confirms the concentration-dependent nature of both D_t and α. Simply treating these variables as constants instead leads to poor fittings to the experimental data as shown in Figure S12. Fickian fitting results under other RH conditions are available in Figure S8. Figure 2c shows the fitted D_t as a function of the normalized concentration under different RH conditions. Corresponding surface permeability results are plotted in Figure S9. Quantitative analysis by Fickian fitting reveals that when RH $\leq$ 50%, D_t is mainly in the range of 10^{-14} to 10^{-11}

m^2/s (Figure 2c). When RH ≥ 60%, the transport diffusivity of DMMP ranges from 10^{-11} to 10^{-10}, increasing by at least one order of magnitude compared to the values at low RH, even though the pores are full of water molecules at high RH (Figure 2d).[15] The shaded area (Figure 2c) highlights the distinguished D_t distribution under different humidities. This observation is somewhat counterintuitive, as one might expect the diffusivity of DMMP to be diminished when the pores are full of water molecules due to simple steric hindrance in the pores. These results indicate that the intracrystalline diffusion mechanism in this system is more complex than steric confinement.[26,60,61]

We also determined the rate-limiting step (transport diffusion versus surface permeation) in this process using the dimensionless parameter $\frac{l\alpha}{D_t}$.[36,37] According to Heinke and Kärger,[37] $\frac{l\alpha}{D_t} > 100$ indicates that intracrystalline diffusion is the rate-limiting step, $\frac{l\alpha}{D_t} < 0.01$ indicates that the transport is dominated by the surface barriers, and $\frac{l\alpha}{D_t} \approx 1$ suggests that both diffusion and surface barriers contribute to the overall resistance. In our case, we found that the value of $\frac{l\alpha}{D_t}$ is in the range of 0.1 to 10 (Figure S10), implying that both contributions must be considered in describing the transport. Fickian analysis on an independent set of the experiments confirmed that these results are reproducible (Figure S11).

DMMP Diffusion under Equilibrium Conditions by MAS NMR. A systemic study using ^{1}H and ^{31}P MAS NMR was carried out to understand the static and dynamic behavior of water and DMMP within NU-1008 at equilibrium. First, the ^{1}H NMR spectra of NU-1008 under different RH values in Figure 3a provided information on the interactions between Zr$_6$ nodes and water. As RH increases, the peak at 2.0 ppm, which corresponds to the proton from the −OH group on the Zr$_6$ nodes, shifts downfield, indicating H-bond formation with H$_2$O molecules. In addition, new peaks at ∼4.0 and ∼5.3 ppm appear after water adsorption, which correspond to mobile water molecules in the pores and H-bonded water on the nodes, respectively (Figure 3a).[62] Note that the mobile H$_2$O peak rises tremendously when RH ≥60%, consistent with the water isotherm (Figure 2d).

^{31}P NMR was next used to examine DMMP under different RH values. At 0% RH, the chemical shift of DMMP adsorbed in NU-1008 (32.1 ppm) is slightly up field compared to that of pure DMMP (32.5 ppm, Figure 3b), which is due to the ring effect from the linkers.[63] With increasing RH, the chemical shift gradually moves downfield, which is consistent with the trend of diluting DMMP with water (Figure 3b). This suggests that when water fills the NU-1008 channels, DMMP molecules are surrounded by water molecules, and the chemical environment of the DMMP molecules in the channel is comparable to that in the bulk DMMP aqueous solution.[64] More details are discussed in Section 3.4 by MD simulation. In addition, as the transverse relaxation time (T_2) of a nucleus has been reported to be sensitive to the mobility of molecules,[65,66] we also measured the T_2 of the ^{31}P nuclei to investigate the mobility of DMMP in the pores at equilibrium. When DMMP is adsorbed in NU-1008, T_2 is in the range of 3−13 ms depending on RH, which is more than 100-fold shorter than DMMP in bulk (Figure S13), indicating restricted mobility due to pore confinement.[67] The RH dependence of T_2 for DMMP

in NU-1008 is complicated and not yet fully understood. Further investigation is needed to elucidate the underlying mechanisms (see the Supporting Information for details). Note that the crystallinity of NU-1008 was maintained after adsorption of DMMP under varying relative humidity as shown by the PXRD patterns (Figure S3).

Molecular-Level Understanding of DMMP Diffusion by Molecular Dynamics Simulations. To provide additional molecular-level insights into the transport and NMR results discussed above, we performed equilibrium MD simulations under three representative RH conditions, i.e., RH = 0, 20, and 70%. Figure 4a shows representative configurations for each RH at low loading of DMMP. At 0% RH, no water molecules are present in the system, and DMMP molecules are preferentially adsorbed on the Zr node. The situation at 20% RH is similar to that at 0% RH but with a few water molecules present in the system, mostly near the Zr nodes. At 70% RH, micropores in NU-1008 are full and the mesopores are partially filled by water molecules.

Figure 4b shows the self-diffusivity D_s of DMMP in the meso-channel of NU-1008 under equilibrium conditions as a function of loading. The diffusion in the meso-channel can best represent the diffusion behavior observed in experiments because (1) the windows between the mesopore and the micropore are too small (Figure 1) for DMMP molecules to freely pass through and (2) the meso-channel accounts for about 90% of the total adsorption capacity of DMMP in NU-1008. First, we studied D_s at infinite dilution of DMMP, where D_s and D_t are equivalent.[51] As shown in Figure 4b, we found that, for 70% RH, the value of D_s at low loading of DMMP is several orders of magnitude higher than that at 0 and 20% RH, which is consistent with the general trend of D_t drawn from the Fickian analysis in Figure 2c, i.e., high RH assists the diffusion of DMMP.

At low loadings of DMMP at 0 and 20% RH, the channels are nearly empty, and the MD trajectories reveal that DMMP molecules tend to stick to the Zr nodes during the entire simulation (Figure 4a,c) through hydrogen bonding with a hydrogen atom in the terminal hydroxyl group (OH−), bridging hydroxyl group (Zr−OH−Zr), or bound water (H$_2$O−) on the nodes. The hydrogen bonding can be seen in the radial distribution function (RDF) between the hydrogen atoms in the Zr node and the (O═P) oxygen atoms in DMMP in Figure 4d. The RDF, $g(r)$, was calculated by the MDAnalysis package,[68] and it measures the probability of finding a particle at a radial distance r from a given reference particle, relative to that for an ideal gas.[69] The RDFs for RH = 0 and 20% exhibit a prominent peak at ∼2 Å, which corresponds to hydrogen bonding between the DMMP molecules and hydrogen atoms in the aforementioned groups on the nodes. In contrast, when the meso-channel is (partially) filled with water at RH = 70%, DMMP molecules form hydrogen bonds mostly with surrounding water molecules. The strong tendency of DMMP to form hydrogen bonds with free water molecules was also observed in DMMP/water bulk mixtures (Figure S18).[70] The RDF for RH = 70% in Figure 4d shows no pronounced peak at 2 Å, suggesting that hydrogen bonds between DMMP and the Zr nodes are absent, and this causes DMMP to be more mobile in this case. We note that the simulation results are based on a bare Zr node structure without formate groups (structure in Figure S14a) due to the tendency of formate to dissolve in water (Figure 3a). For Zr nodes with three formates (structure in Figure S14b), the RDF

in Figure S20 shows that hydrogen bonding still exists due to the interaction between the oxygen atom in DMMP and the hydrogen atom in (Zr−OH−Zr) segments of the node.

Figure 4b shows that, as the loading of DMMP increases, the self-diffusivity varies, albeit in a complex fashion. Note that, for simplicity, in Figure 4b, the concentration of DMMP in NU-1008 was varied, while the number of H_2O molecules was fixed for a given RH. In reality, H_2O and DMMP might exhibit competitive adsorption. Figure 4b shows that, as the number of DMMP molecules increases up to 6 per node ($\rho_{free} \approx 0.5$ g/cc) for RH = 0 and 20%, the self-diffusivity increases. At 6 DMMP per node, the adsorption sites on the node are saturated (Figure S21), and there is an inflection in the self-diffusivity curve. Beyond the inflection point, the self-diffusivity continues to increase with loading as further DMMP molecules added to the system can freely diffuse in the center of the meso-channel without being restricted to the adsorption sites on the node. At high loading ($\rho_{free} > 1.17$ g/cc), the mobility of DMMP drops with increasing loading due in part to a reduction of the free volume in the meso-channel. In contrast, the diffusion profile for RH = 70% presents a monotonically decreasing trend due to the reduction of the free volume and the formation of small aggregates, which are discussed below.

Another interesting observation in Figure 4b is that, at low DMMP loading, the DMMP self-diffusivity is the highest at 70% RH, while at the highest DMMP loading (vertical dashed line in Figure 4b), the DMMP self-diffusivity is the lowest at 70% RH compared to 0 and 20% RH. To better understand the DMMP loading effect in pores that are full of water molecules, we further investigated the DMMP−DMMP interactions in NU-1008 and in bulk aqueous solution. Vishnyakov et al.[70] performed molecular dynamics simulations to understand the behavior of DMMP in bulk aqueous solutions. They found that DMMP forms small aggregates in its dilute solutions due to its hydrophobic nature. Such clustering was found to have opposite effects on D_s of DMMP molecules, leading to lower D_s compared to that of the pure DMMP solution. Our molecular dynamics simulations of bulk DMMP/water mixture confirm their findings (Section S6.5). Interestingly, we found the formation of similar DMMP aggregates in the meso-channel in NU-1008 at 70% RH as shown in Figure 4e. The DMMP aggregate size was estimated by a clustering algorithm. That is, if the pairwise distance between a target DMMP molecule and any molecules in a cluster is smaller than a certain cutoff, that target DMMP molecule was considered to belong to that cluster. A cutoff radius of 6.425 Å was chosen; below this value, the algorithm is unable to cluster the pure DMMP liquid (at 298 K and 1 bar) as a single "aggregate". Figure 4e shows that the size of the DMMP aggregates increases with the concentration of DMMP in the meso-channel, consistent with the behavior in the bulk aqueous solution. This suggests that the chemical environment of DMMP in NU-1008 at high RH is similar to that in the bulk DMMP aqueous solution, corroborating the MAS NMR results in Figure 3b. The difference is that the DMMP molecules (or aggregates) in NU-1008 are jumping between organic linkers due to favorable interactions (as observed from simulation trajectories) and experience the confinement of the channels, while DMMP in the bulk solution can freely diffuse.

CONCLUSIONS

In situ assessments of the transient uptake of the nerve agent simulant (DMMP) by the Zr-MOF NU-1008 can be accomplished via confocal Raman microscopy. The non-equilibrium transport diffusivity of DMMP at high RH (channels filled with water) is observed to be higher than at low RH. This counterintuitive finding implies that DMMP transport in NU-1008 is influenced not only by steric hindrance but also by host−guest and specific guest−guest interactions. To gain a molecular level understanding of the mechanism, a MAS NMR study of DMMP in NU-1008 under equilibrium conditions was performed, which suggests that DMMP, surrounded by water at higher RH, engages in solvated diffusion and therefore displays higher mobility. Molecular dynamics simulations facilitate the understanding of non-equilibrium and equilibrium diffusion results, where, at high RH (70% RH), water molecules form hydrogen bonding with the nodes and diminish strong interactions between the aqua/hydroxo-ligated Zr nodes and DMMP molecules, thus enhancing DMMP transport. Additionally, MD simulations reveal that DMMP molecules, depending on loading, can form clusters in NU-1008 at high RH due to their hydrophobicity—behavior that translates to smaller self-diffusivities and less mobility under saturation conditions. This investigation provides a new understanding of vapor-phase nerve agent diffusion in Zr-MOFs in the presence of humidity. These findings will facilitate the future work aimed at elucidating the dynamics of nerve agent reaction within Zr-MOFs and further aid the design of superior Zr-MOF-based materials for human protection.

ASSOCIATED CONTENT

Ⓢ Supporting Information

The Supporting Information is available free of charge at https://pubs.acs.org/doi/10.1021/jacs.3c03708.

> Experimental procedures, powder X-ray diffraction patterns, N_2 isotherm, pore size distribution, DRIFTS, Raman spectra, NMR spectra, fitting details, and simulation details (PDF)

> Jupyter notebook for performing Fickian diffusion fittings, example simulation input and output files, and Python scripts for simulation analysis (ZIP)

AUTHOR INFORMATION

Corresponding Authors

Randall Q. Snurr − *Department of Chemical and Biological Engineering, Northwestern University, Evanston, Illinois 60208, United States;* ⓞ orcid.org/0000-0003-2925-9246; Email: snurr@northwestern.edu

Joseph T. Hupp − *Department of Chemistry, Northwestern University, Evanston, Illinois 60208, United States;* ⓞ orcid.org/0000-0003-3982-9812; Email: j-hupp@ northwestern.edu

Authors

Rui Wang − *Department of Chemistry, Northwestern University, Evanston, Illinois 60208, United States;* ⓞ orcid.org/0000-0001-9833-2115

Kaihang Shi − *Department of Chemical and Biological Engineering, Northwestern University, Evanston, Illinois 60208, United States*

Jian Liu − *Department of Chemistry, Northwestern University, Evanston, Illinois 60208, United States; School of Chemistry and Materials Science, Rochester Institute of Technology,*

Rochester, New York 14623, United States; ● orcid.org/
0000-0002-5024-1879

Complete contact information is available at:
https://pubs.acs.org/10.1021/jacs.3c03708

Author Contributions

‖R.W. and K.S. contributed equally to this work.

Author Contributions

All authors have given approval to the final version of the manuscript.

Notes

The authors declare the following competing financial interest(s): Randall Q. Snurr. and Joseph T. Hupp have equity interests in NuMat Technologies, a company that commercializes metal-organic frameworks.

■ REFERENCES

(1) Furukawa, H.; Cordova, K. E.; O'Keeffe, M.; Yaghi, O. M. The Chemistry and Applications of Metal-Organic Frameworks. *Science* **2013**, *341*, No. 1230444.

(2) Wang, Q.; Yang, G.; Fu, Y.; Li, N.; Hao, D.; Ma, S. Nanospace Engineering of Metal-Organic Frameworks for Heterogeneous Catalysis. *ChemNanoMat* **2022**, *8*, 1−19.

(3) Liu, J.; Yang, Y.; Goetjen, T. A.; Hupp, J. T. Carbon-Efficient Conversion of Natural Gas and Natural-Gas Condensates to Chemical Products and Intermediate Feedstocks via Catalytic Metal−Organic Framework (MOF) Chemistry. *Energy Environ. Sci.* **2022**, *15*, 2819−2842.

(4) Kirlikovali, K. O.; Chen, Z.; Islamoglu, T.; Hupp, J. T.; Farha, O. K. Zirconium-Based Metal-Organic Frameworks for the Catalytic Hydrolysis of Organophosphorus Nerve Agents. *ACS Appl. Mater. Interfaces* **2020**, *12*, 14702−14720.

(5) Vellingiri, K.; Philip, L.; Kim, K. H. Metal−Organic Frameworks as Media for the Catalytic Degradation of Chemical Warfare Agents. *Coord. Chem. Rev.* **2017**, *353*, 159−179.

(6) Gao, W. Y.; Cardenal, A. D.; Wang, C. H.; Powers, D. C. In Operando Analysis of Diffusion in Porous Metal-Organic Framework Catalysts. *Chem. - Eur. J.* **2019**, *25*, 3465−3476.

(7) Liu, J.; Goetjen, T. A.; Wang, Q.; Knapp, J. G.; Wasson, M. C.; Yang, Y.; Syed, Z. H.; Delferro, M.; Notestein, J. M.; Farha, O. K.; Hupp, J. T. MOF-Enabled Confinement and Related Effects for Chemical Catalyst Presentation and Utilization. *Chem. Soc. Rev.* **2022**, *51*, 1045−1097.

(8) Jacoby, M. Heading To Market. *Chem. Eng. News* **2008**, *86*, 13−16.

(9) Mueller, U.; Schubert, M.; Teich, F.; Puetter, H.; Schierle-Arndt, K.; Pastré, J. Metal-Organic Frameworks - Prospective Industrial Applications. *J. Mater. Chem.* **2006**, *16*, 626−636.

(10) Chmelik, C. Characteristic Features of Molecular Transport in MOF ZIF-8 as Revealed by IR Microimaging. *Microporous Mesoporous Mater.* **2015**, *216*, 138−145.

(11) Sharp, C. H.; Bukowski, B. C.; Li, H.; Johnson, E. M.; Ilic, S.; Morris, A. J.; Gersappe, D.; Snurr, R. Q.; Morris, J. R. Nanoconfinement and Mass Transport in Metal−Organic Frameworks. *Chem. Soc. Rev.* **2021**, *50*, 11530−11558.

(12) Hanikel, N.; Pei, X.; Chheda, S.; Lyu, H.; Jeong, W.; Sauer, J.; Gagliardi, L.; Yaghi, O. M. Evolution of Water Structures in Metal-Organic Frameworks for Improved Atmospheric Water Harvesting. *Science* **2021**, *459*, 454−459.

(13) Chen, Z.; Ma, K.; Mahle, J. J.; Wang, H.; Syed, Z. H.; Atilgan, A.; Chen, Y.; Xin, J. H.; Islamoglu, T.; Peterson, G. W.; Farha, O. K. Integration of Metal-Organic Frameworks on Protective Layers for Destruction of Nerve Agents under Relevant Conditions. *J. Am. Chem. Soc.* **2019**, *141*, 20016−20021.

(14) Lawrence, M. C.; Katz, M. J. Analysis of the Water Adsorption Isotherms in UiO-Based Metal−Organic Frameworks. *J. Phys. Chem. C* **2022**, *126*, 1107−1114.

(15) Lu, Z.; Duan, J.; Tan, H.; Du, L.; Zhao, X.; Wang, R.; Kato, S.; Yang, S.; Hupp, J. T. Isomer of NU-1000 with a Blocking c-Pore Exhibits High Water-Vapor Uptake Capacity and Greatly Enhanced Cycle Stability. *J. Am. Chem. Soc.* **2023**, *145*, 4150−4157.

(16) Zheng, Z.; Hanikel, N.; Lyu, H.; Yaghi, O. M. Broadly Tunable Atmospheric Water Harvesting in Multivariate Metal-Organic Frameworks. *J. Am. Chem. Soc.* **2022**, *144*, 22669−22675.

(17) Towsif Abtab, S. M.; Alezi, D.; Bhatt, P. M.; Shkurenko, A.; Belmabkhout, Y.; Aggarwal, H.; Weseliński, Ł. J.; Alsadun, N.; Samin, U.; Hedhili, M. N.; Eddaoudi, M. Reticular Chemistry in Action: A Hydrolytically Stable MOF Capturing Twice Its Weight in Adsorbed Water. *Chem* **2018**, *4*, 94−105.

(18) Mondloch, J. E.; Katz, M. J.; Isley, W. C.; Ghosh, P.; Liao, P.; Bury, W.; Wagner, G. W.; Hall, M. G.; Decoste, J. B.; Peterson, G. W.; Snurr, R. Q.; Cramer, C. J.; Hupp, J. T.; Farha, O. K. Destruction of Chemical Warfare Agents Using Metal-Organic Frameworks. *Nat. Mater.* **2015**, *14*, 512−516.

(19) Liu, Y.; Howarth, A. J.; Vermeulen, N. A.; Moon, S. Y.; Hupp, J. T.; Farha, O. K. Catalytic Degradation of Chemical Warfare Agents and Their Simulants by Metal-Organic Frameworks. *Coord. Chem. Rev.* **2017**, *346*, 101−111.

(20) Ma, K.; Islamoglu, T.; Chen, Z.; Li, P.; Wasson, M. C.; Chen, Y.; Wang, Y.; Peterson, G. W.; Xin, J. H.; Farha, O. K. Scalable and Template-Free Aqueous Synthesis of Zirconium-Based Metal-Organic Framework Coating on Textile Fiber. *J. Am. Chem. Soc.* **2019**, *141*, 15626−15633.

(21) Moon, S. Y.; Proussaloglou, E.; Peterson, G. W.; DeCoste, J. B.; Hall, M. G.; Howarth, A. J.; Hupp, J. T.; Farha, O. K. Detoxification of Chemical Warfare Agents Using a Zr6-Based Metal−Organic Framework/Polymer Mixture. *Chem. - Eur. J.* **2016**, *22*, 14864−14868.

(22) Peterson, G. W.; Lee, D. T.; Barton, H. F.; Epps, T. H.; Parsons, G. N. Fibre-Based Composites from the Integration of Metal−Organic Frameworks and Polymers. *Nat. Rev. Mater.* **2021**, *6*, 605−621.

(23) Plonka, A. M.; Grissom, T. G.; Musaev, D. G.; Balboa, A.; Gordon, W. O.; Collins-Wildman, D. L.; Ghose, S. K.; Tian, Y.; Ebrahim, A. M.; Mitchell, M. B.; Hill, C. L.; Morris, J. R.; Frenkel, A. I. Effect of Carbon Dioxide on the Degradation of Chemical Warfare Agent Simulant in the Presence of Zr Metal Organic Framework MOF-808. *Chem. Mater.* **2019**, *31*, 9904−9914.

(24) Wang, G.; Sharp, C.; Plonka, A. M.; Wang, Q.; Frenkel, A. I.; Guo, W.; Hill, C.; Smith, C.; Kollar, J.; Troya, D.; Morris, J. R. Mechanism and Kinetics for Reaction of the Chemical Warfare Agent Simulant, DMMP(g), with Zirconium(IV) MOFs: An Ultrahigh-Vacuum and DFT Study. *J. Phys. Chem. C* **2017**, *121*, 11261−11272.

(25) Wang, H.; Mahle, J. J.; Tovar, T. M.; Peterson, G. W.; Hall, M. G.; Decoste, J. B.; Buchanan, J. H.; Karwacki, C. J. Solid-Phase Detoxification of Chemical Warfare Agents Using Zirconium-Based Metal Organic Frameworks and the Moisture Effects: Analyze via Digestion. *ACS Appl. Mater. Interfaces* **2019**, *11*, 21109−21116.

(26) Shahraeeni, E.; Or, D. Pore Scale Mechanisms for Enhanced Vapor Transport through Partially Saturated Porous Media. *Water Resour. Res.* **2012**, *48*, 1−16.

(27) Wang, R.; Bukowski, B. C.; Duan, J.; Sheridan, T. R.; Atilgan, A.; Zhang, K.; Snurr, R. Q.; Hupp, J. T. Investigating the Process and Mechanism of Molecular Transport within a Representative Solvent-Filled Metal-Organic Framework. *Langmuir* **2020**, *36*, 10853−10859.

(28) Agrawal, M.; Boulfelfel, S. E.; Sava Gallis, D. F.; Greathouse, J. A.; Sholl, D. S. Determining Diffusion Coefficients of Chemical Warfare Agents in Metal-Organic Frameworks. *J. Phys. Chem. Lett.* **2019**, *10*, 7823−7830.

(29) Bryce, D. A.; Kitt, J. P.; Harris, J. M. Confocal Raman Microscopy Investigation of Molecular Transport into Individual Chromatographic Silica Particles. *Anal. Chem.* **2017**, *89*, 2755−2763.

(30) Chen, Y.; Hong, S.; Fu, C. W.; Hoang, T.; Li, X.; Valencia, V.; Zhang, Z.; Perman, J. A.; Ma, S. Investigation of the Mesoporous Metal-Organic Framework as a New Platform to Study the Transport Phenomena of Biomolecules. *ACS Appl. Mater. Interfaces* **2017**, *9*, 10874−10881.

(31) Rivera-Torrente, M.; Filez, M.; Schneider, C.; Van Der Feltz, E. C.; Wolkersdörfer, K.; Taffa, D. H.; Wark, M.; Fischer, R. A.; Weckhuysen, B. M. Micro-Spectroscopy of HKUST-1 Metal-Organic Framework Crystals Loaded with Tetracyanoquinodimethane: Effects of Water on Host-Guest Chemistry and Electrical Conductivity. *Phys. Chem. Chem. Phys.* **2019**, *21*, 25678−25689.

(32) Yi, X.; Ko, H. H.; Deng, F.; Liu, S. B.; Zheng, A. Solid-State 31P NMR Mapping of Active Centers and Relevant Spatial Correlations in Solid Acid Catalysts. *Nat. Protoc.* **2020**, *15*, 3527−3555.

(33) Bornes, C.; Fischer, M.; Amelse, J. A.; Geraldes, C. F. G. C.; Rocha, J.; Mafra, L. What Is Being Measured with P-Bearing NMR Probe Molecules Adsorbed on Zeolites? *J. Am. Chem. Soc.* **2021**, *143*, 13616−13623.

(34) Jellen, M. J.; Jiang, X.; Benders, S.; Adams, A.; Garcia-Garibay, M. A. Slip/Stick Viscosity Models of Nanoconfined Liquids: Solvent-Dependent Rotation in Metal-Organic Frameworks. *J. Org. Chem.* **2022**, *87*, 1780−1790.

(35) Titze, T.; Lauerer, A.; Heinke, L.; Chmelik, C.; Zimmermann, N. E. R.; Keil, F. J.; Ruthven, D. M.; Kärger, J. Transport in Nanoporous Materials Including MOFs: The Applicability of Fick's Laws. *Angew. Chem., Int. Ed.* **2015**, *54*, 14580−14583.

(36) Crank, J. *The Mathematics of Diffusion*. Oxford University Press, 1975.

(37) Heinke, L.; Kärger, J. Assessing One-Dimensional Diffusion in Nanoporous Materials from Transient Concentration Profiles. *New J. Phys.* **2008**, *10*, No. 023035.

(38) Plimpton, S. Fast Parallel Algorithms for Short-Range Molecular Dynamics. *J. Comput. Phys.* **1995**, *11*, 1−19.

(39) Basconi, J. E.; Shirts, M. R. Effects of Temperature Control Algorithms on Transport Properties and Kinetics in Molecular Dynamics Simulations. *J. Chem. Theory Comput.* **2013**, *9*, 2887−2899.

(40) Sokkalingam, N.; Kamath, G.; Coscione, M.; Potoff, J. J. Extension of the Transferable Potentials for Phase Equilibria Force Field to Dimethylmethyl Phosphonate, Sarin, and Soman. *J. Phys. Chem. B* **2009**, *113*, 10292−10297.

(41) Emelianova, A.; Basharova, E. A.; Kolesnikov, A. L.; Arribas, E. V.; Ivanova, E. V.; Gor, G. Y. Force Fields for Molecular Modeling of Sarin and Its Simulants: DMMP and DIMP. *J. Phys. Chem. B* **2021**, *125*, 4086−4098.

(42) Abascal, J. L. F.; Vega, C. A General Purpose Model for the Condensed Phases of Water: TIP4P/2005. *J. Chem. Phys.* **2005**, *123*, 234505.

(43) Mayo, S. L.; Olafson, B. D.; Goddard, W. A. DREIDING: A Generic Force Field for Molecular Simulations. *J. Phys. Chem.* **1990**, *94*, 8897−8909.

(44) Rappe, A. K.; Casewit, C. J.; Colwell, K. S.; Goddard, W. A.; Skiff, W. M. UFF, a Full Periodic Table Force Field for Molecular Mechanics and Molecular Dynamics Simulations. *J. Am. Chem. Soc.* **1992**, *114*, 10024−10035.

(45) Chen, B.; Potoff, J. J.; Siepmann, J. I. Monte Carlo Calculations for Alcohols and Their Mixtures with Alkanes. Transferable Potentials for Phase Equilibria. 5. United-Atom Description of Primary, Secondary, and Tertiary Alcohols. *J. Phys. Chem. B* **2002**, *105*, 3093−3104.

(46) Wardzala, J. J.; Ruffley, J. P.; Goodenough, I.; Schmidt, A. M.; Shukla, P. B.; Wei, X.; Bagusetty, A.; De Souza, M.; Das, P.; Thompson, D. J.; Karwacki, C. J.; Wilmer, C. E.; Borguet, E.; Rosi, N. L.; Johnson, J. K. Modeling of Diffusion of Acetone in UiO-66. *J. Phys. Chem. C* **2020**, *124*, 28469−28478.

(47) Kancharlapalli, S.; Gopalan, A.; Haranczyk, M.; Snurr, R. Q. Fast and Accurate Machine Learning Strategy for Calculating Partial Atomic Charges in Metal-Organic Frameworks. *J. Chem. Theory Comput.* **2021**, *17*, 3052−3064.

(48) Hockney, R. W.; Eastwood, J. W. *Computer Simulation Using Particles*. Taylor & Francis, Inc, 1988.

(49) Allen, M. P.; Tildesley, D. J. *Computer Simulation of Liquids*. Oxford University Press, 2017, 216−257.

(50) Dubbeldam, D.; Calero, S.; Ellis, D. E.; Snurr, R. Q. RASPA: Molecular Simulation Software for Adsorption and Diffusion in Flexible Nanoporous Materials. *Mol. Simul.* **2016**, *42*, 81−101.

(51) Xu, H.; Cabriolu, R.; Smit, B. Effects of Degrees of Freedom on Calculating Diffusion Properties in Nanoporous Materials. *J. Chem. Theory Comput.* **2022**, *18*, 2826−2835.

(52) Vargas, L.; Snurr, R. Q. Heterogeneous Diffusion of Alkanes in the Hierarchical Metal-Organic Framework NU-1000. *Langmuir* **2015**, *31*, 10056−10065.

(53) Lyu, J.; Zhang, X.; Otake, K. I.; Wang, X.; Li, P.; Li, Z.; Chen, Z.; Zhang, Y.; Wasson, M. C.; Yang, Y.; Bai, P.; Guo, X.; Islamoglu, T.; Farha, O. K. Topology and Porosity Control of Metal-Organic Frameworks through Linker Functionalization. *Chem. Sci.* **2019**, *10*, 1186−1192.

(54) Planas, N.; Mondloch, J. E.; Tussupbayev, S.; Borycz, J.; Gagliardi, L.; Hupp, J. T.; Farha, O. K.; Cramer, C. J. Defining the Proton Topology of the Zr 6-Based Metal{\textendash}Organic Framework NU-1000. *J. Phys. Chem. Lett.* **2014**, *5*, 3716−3723.

(55) Yang, D.; Ortuño, M. A.; Bernales, V.; Cramer, C. J.; Gagliardi, L.; Gates, B. C. Structure and Dynamics of Zr6O8 Metal-Organic Framework Node Surfaces Probed with Ethanol Dehydration as a Catalytic Test Reaction. *J. Am. Chem. Soc.* **2018**, *140*, 3751−3759.

(56) Lu, Z.; Liu, J.; Zhang, X.; Liao, Y.; Wang, R.; Zhang, K.; Lyu, J.; Farha, O. K.; Hupp, J. T. Node-Accessible Zirconium MOFs. *J. Am. Chem. Soc.* **2020**, *142*, 21110−21121.

(57) Klet, R. C.; Liu, Y.; Wang, T. C.; Hupp, J. T.; Farha, O. K. Evaluation of Brønsted Acidity and Proton Topology in Zr- and Hf-Based Metal-Organic Frameworks Using Potentiometric Acid-Base Titration. *J. Mater. Chem. A* **2016**, *4*, 1479−1485.

(58) Wang, Q.; Chapleski, R. C.; Plonka, A. M.; Gordon, W. O.; Guo, W.; Nguyen-Phan, T. D.; Sharp, C. H.; Marinkovic, N. S.; Senanayake, S. D.; Morris, J. R.; Hill, C. L.; Troya, D.; Frenkel, A. I. Atomic-Level Structural Dynamics of Polyoxoniobates during DMMP Decomposition. *Sci. Rep.* **2017**, *7*, 1−8.

(59) Hibbe, F.; Chmelik, C.; Heinke, L.; Pramanik, S.; Li, J.; Ruthven, D. M.; Tzoulaki, D.; Kärger, J. The Nature of Surface Barriers on Nanoporous Solids Explored by Microimaging of Transient Guest Distributions. *J. Am. Chem. Soc.* **2011**, *133*, 2804−2807.

(60) Gordon, W. O.; Tissue, B. M.; Morris, J. R. Adsorption and Decomposition of Dimethyl Methylphosphonate on Y 2O3 Nanoparticles. *J. Phys. Chem. C* **2007**, *111*, 3233−3240.

(61) Knagge, K.; Johnson, M.; Grassian, V. H.; Larsen, S. C. Adsorption and Thermal Reaction of DMMP in Nanocrystalline NaY. *Langmuir* **2006**, *22*, 11077−11084.

(62) Trickett, C. A.; Osborn Popp, T. M.; Su, J.; Yan, C.; Weisberg, J.; Huq, A.; Urban, P.; Jiang, J.; Kalmutzki, M. J.; Liu, Q.; Baek, J.; Head-Gordon, M. P.; Somorjai, G. A.; Reimer, J. A.; Yaghi, O. M. Identification of the Strong Brønsted Acid Site in a Metal−Organic Framework Solid Acid Catalyst. *Nat. Chem.* **2019**, *11*, 170−176.

(63) Nandy, A.; Forse, A. C.; Witherspoon, V. J.; Reimer, J. A. NMR Spectroscopy Reveals Adsorbate Binding Sites in the Metal-Organic Framework UiO-66(Zr). *J. Phys. Chem. C* **2018**, *122*, 8295−8305.

(64) Sambur, J. B.; Doetschman, D. C.; Yang, S. W.; Schulte, J. T.; Jones, B. R.; DeCoste, J. B. Multiple Effects of the Presence of Water on the Nucleophilic Substitution Reactions of NaX Faujasite Zeolite with Dimethyl Methylphosphonate (DMMP). *Microporous Mesoporous Mater.* **2008**, *112*, 116−124.

(65) D'Agostino, C.; Mitchell, J.; Mantle, M. D.; Gladden, L. F. Interpretation of NMR Relaxation as a Tool for Characterising the Adsorption Strength of Liquids inside Porous Materials. *Chem. - Eur. J.* **2014**, *20*, 13009−13015.

(66) Mitchell, J.; Broche, L. M.; Chandrasekera, T. C.; Lurie, D. J.; Gladden, L. F. Exploring Surface Interactions in Catalysts Using Low-Field Nuclear Magnetic Resonance. *J. Phys. Chem. C* **2013**, *117*, 17699−17706.

(67) Marreiros, J.; de Oliveira-Silva, R.; Iacomi, P.; Llewellyn, P. L.; Ameloot, R.; Sakellariou, D. Benchtop In Situ Measurement of Full Adsorption Isotherms by NMR. *J. Am. Chem. Soc.* **2021**, *143*, 8249−8254.

(68) Michaud-Agrawal, N.; Denning, E. J.; Woolf, T. B.; Beckstein, O. MDAnalysis: A Toolkit for the Analysis of Molecular Dynamics Simulations. *J. Comput. Chem.* **2011**, *32*, 2319−2327.

(69) Frenkel, D.; Smit, B. *Understanding Molecular Simulation: From Algorithms to Applications*. Academic Press, 2002.

(70) Vishnyakov, A.; Gor, G. Y.; Lee, M.-T.; Neimark, A. V. Molecular Modeling of Organophosphorous Agents and Their Aqueous Solutions. *J. Phys. Chem. A* **2011**, *115*, 5201−5209.